Supplementary information

The visual appearances of disordered optical metasurfaces

In the format provided by the authors and unedited

Supplementary Information for "The visual appearances of disordered optical metasurfaces"

Kevin Vynck,[1, *] Romain Pacanowski,[1, 2] Adrian Agreda,[1] Arthur Dufay,[2] Xavier Granier,[1] and Philippe Lalanne[1, †]

[1]*Univ. Bordeaux, IOGS, CNRS, LP2N, F-33400 Talence, France*
[2]*INRIA Bordeaux Sud-Ouest, F-33400 Talence, France*

CONTENTS

* kevin.vynck@univ-lyon1.fr; Current address: Univ. Claude Bernard Lyon 1, CNRS, iLM, F-69622 Villeurbanne Cedex, France
† philippe.lalanne@institutoptique.fr

SUPPLEMENTARY NOTE 1. BRDF MODEL FOR DISORDERED METASURFACES

The method used in the main text to predict the visual appearance of macroscopic objects requires the knowledge of the BRDF of disordered metasurfaces. We tackle here a longstanding issue with the modelling of random scattering surfaces. The difficulty to model disordered metasurfaces comes from the need to take into account not only the intricate coherent phenomena occurring at the scale of a few particles (high-index resonances of individual particles, interaction with a layered substrate, mutual interaction between particles in a correlated disorder) but also the fact that the disordered metasurface covers very large areas, much larger than a few wavelength squared.

Here, we present an approximate BRDF model that relies on both full-wave electromagnetic computations to predict the scattering by an individual particle on a layered substrate and electromagnetic scattering theory to predict the optical response of a virtually infinite surface made of such scatterers. As classically done, the multiple scattering by ensembles of particles is described perturbatively [S1] and leads to corrections to the radiative properties obtained with the independent scattering approximation (ISA) wherein the mutual interaction between particles is neglected. The strength of the model, which is used to create the rendered images of the present work, is that it disentangles the respective roles of individual particles and of structural correlations on the diffuse intensity, thereby providing considerable insight on the control knobs for visual appearance.

We start by introducing the notions of coherent and incoherent intensities and then describe the approach employed in the present work to compute the specular and diffuse components of the BRDF.

Coherent and incoherent intensity

We consider an ensemble of N particles incorporated in a planar stratified medium. All materials are assumed to be non-magnetic (relative permeability, $\mu(\mathbf{r}) = 1$). We further consider harmonic fields at frequency ω with the $e^{-i\omega t}$ convention and drop the explicit time dependence for simplicity. From Maxwell's equations, one shows that the scattered electric field $\mathbf{E}_{\mathrm{s}}(\mathbf{r})$ produced by the system for an arbitrary background field $\mathbf{E}_{\mathrm{b}}(\mathbf{r})$ is described by a set of two equations, as [S1, S2]

$$\mathbf{E}_{\mathrm{s}}(\mathbf{r}) = \sum_p \int \mathbf{G}_{\mathrm{b}}(\mathbf{r},\mathbf{r}')\mathbf{T}_p(\mathbf{r}'-\mathbf{r}_p,\mathbf{r}''-\mathbf{r}_p)\mathbf{E}_{\mathrm{exc}}^p(\mathbf{r}'')d\mathbf{r}'d\mathbf{r}'', \tag{S1}$$

$$\mathbf{E}_{\mathrm{exc}}^p(\mathbf{r}) = \mathbf{E}_{\mathrm{b}}(\mathbf{r}) + \sum_{q\neq p} \int \mathbf{G}_{\mathrm{b}}(\mathbf{r},\mathbf{r}')\mathbf{T}_q(\mathbf{r}'-\mathbf{r}_q,\mathbf{r}''-\mathbf{r}_q)\mathbf{E}_{\mathrm{exc}}^q(\mathbf{r}'')d\mathbf{r}'d\mathbf{r}''. \tag{S2}$$

$\mathbf{T}_p$ is the transition operator of the p-th particle, which relates the field exciting the particle and the polarization density induced in it. It is directly given by Mie theory for particles with spherical symmetry [S3] and can be computed numerically otherwise [S4]. $\mathbf{G}_{\mathrm{b}}$ is the dyadic Green function in the background medium, which describes the electric field produced by a radiating point electric dipole at any point of space [S5]. Equation (S1) states that the total scattered field $\mathbf{E}_{\mathrm{s}}$ is the sum of the field scattered by all particles in the system. Each particle p is excited by a field $\mathbf{E}_{\mathrm{exc}}^p$, which, following Eq. (S2), is the sum of the background field and the field scattered by all other particles $q \neq p$. This system of two equations constitutes a rigorous description of multiple light scattering by assemblies of particles. It is the classical starting point of multiple-scattering theories [S1] and can be solved exactly by computational methods on finite ensembles of particles (as, for instance, to compute the results reported in the Supplementary Note 2).

In the present study, we are interested in determining the optical response of a large (macroscopic) surface illuminated by a partially coherent source (e.g., sunlight) and should therefore look for the statistical properties of the scattered light upon configurational average. For identical particles ($\mathbf{T}_p \equiv \mathbf{T}$), the average is made over the particle positions and is defined as

$$\langle \boldsymbol{g}(\mathbf{r},\boldsymbol{R})\rangle = \int \boldsymbol{g}(\mathbf{r},\boldsymbol{R})p(\boldsymbol{R})d\mathbf{r}_1 d\mathbf{r}_2..., \tag{S3}$$

where $\boldsymbol{g}(\mathbf{r},\boldsymbol{R})$ is a function and $p(\boldsymbol{R})$ is the probability density function of finding the particles in configuration $\boldsymbol{R} = [\mathbf{r}_1, \mathbf{r}_2, ...]$. Decomposing the scattered field as the sum of its average and a fluctuating part, $\mathbf{E}_{\mathrm{s}}(\mathbf{r}) = \langle \mathbf{E}_{\mathrm{s}}(\mathbf{r})\rangle + \delta\mathbf{E}_{\mathrm{s}}(\mathbf{r})$, with $\langle \delta\mathbf{E}_{\mathrm{s}}(\mathbf{r})\rangle = 0$, one can write the average intensity of the total field, $\mathbf{E} = \mathbf{E}_{\mathrm{b}} + \mathbf{E}_{\mathrm{s}}$, as the sum of two terms,

$$\langle |\mathbf{E}(\mathbf{r})|^2 \rangle = |\langle \mathbf{E}(\mathbf{r})\rangle|^2 + \langle |\delta\mathbf{E}_{\mathrm{s}}(\mathbf{r})|^2 \rangle. \tag{S4}$$

The first term, $|\langle \mathbf{E}(\mathbf{r})\rangle|^2$, is the so-called *coherent intensity*, whose propagation in bulk media is assimilated to that in an effective medium with parameters often derived from mixing rules (e.g., Maxwell-Garnett, Bruggeman) [S1]. The second term, $\langle |\delta\mathbf{E}_{\mathrm{s}}(\mathbf{r})|^2 \rangle = \langle |\mathbf{E}_{\mathrm{s}}(\mathbf{r})|^2 \rangle - |\langle \mathbf{E}_{\mathrm{s}}(\mathbf{r})\rangle|^2$, is the so-called *incoherent intensity*, responsible for the diffuse scattering. For statistically translationally-invariant (and thus, laterally infinite) planar media, these two terms respectively yield the specular and diffuse components of the scattered light of interest in the present study.

Specular reflectance model

To determine the specular component of the BRDF of disordered metasurfaces, we employ the state-of-the-art multiple-scattering theory developed in Ref. [S6]. This earlier work derives analytical expressions for the complex reflection and transmission coefficients of a infinitely-large monolayer of identical particles in a uniform background. The effect of the substrate on the specular components is introduced later on.

The reflection and transmission coefficients (for s and p incident and scattered polarizations) upon excitation by a linearly-polarized planewave with amplitude $E_{\rm b}$, wavevector $\mathbf{k}_{\rm i} = k_{\rm b}\hat{\mathbf{k}}_{\rm i}$ and polarization $\hat{\boldsymbol{e}}_{\rm i}$ are respectively defined as

$$\mathbf{r}_{\rm coh}\hat{\boldsymbol{e}}_{\rm i}E_{\rm b} = \langle \mathbf{E}_{\rm s}(\mathbf{r}, \mathbf{k}_{\rm r})\rangle, \quad \mathbf{t}_{\rm coh}\hat{\boldsymbol{e}}_{\rm i}E_{\rm b} = \hat{\boldsymbol{e}}_{\rm i}E_{\rm b} + \langle \mathbf{E}_{\rm s}(\mathbf{r}, \mathbf{k}_{\rm t})\rangle, \tag{S5}$$

where $\mathbf{k}_{\rm r}$ and $\mathbf{k}_{\rm t} \equiv \mathbf{k}_{\rm i}$ are the wavevectors of the specularly reflected and transmitted planewaves. From Eq. (S1), one understands that the key quantity to describe the average scattered field $\langle \mathbf{E}_{\rm s}(\mathbf{r}, \mathbf{k}_{\rm r})\rangle$ is the average excitation field $\langle \mathbf{E}_{\rm exc}^p(\mathbf{r})\rangle$, obtained by averaging Eq. (S2). The method developed by Garcia-Valenzuela *et al.* relies in particular on the ansatz that *the average exciting field is composed of specularly transmitted and reflected planewaves*, see Eqs. (18b) in Ref. [S6], which is perfectly sound considering that the monolayer is statistically invariant by translation and is excited by a planewave.

We introduce the scattering amplitude of a particle in a *homogeneous* medium as

$$\mathbf{A}_p(\mathbf{k}_{\rm s}, \mathbf{k}_{\rm i}) = \frac{1}{4\pi}\left[\mathbf{I} - \hat{\mathbf{k}}_{\rm s} \otimes \hat{\mathbf{k}}_{\rm s}\right]\mathbf{T}_p(\mathbf{k}_{\rm s}, \mathbf{k}_{\rm i}), \tag{S6}$$

where $\mathbf{T}_p(\mathbf{p}', \mathbf{p}'')$ is the Fourier transform of $\mathbf{T}_p(\mathbf{r}' - \mathbf{r}_p, \mathbf{r}'' - \mathbf{r}_p)$ in Eqs. (S1) and (S2), and $\mathbf{k}_{\rm s} = k_{\rm b}\hat{\mathbf{k}}_{\rm s}$ and $\hat{\boldsymbol{e}}_{\rm s}$ are the wavevector and polarization of the scattered planewave. Considering a statistically isotropic and translationally invariant system composed of *identical* spherical particles ($\mathbf{A}_p \equiv \mathbf{A}$), we can neglect the possibility for polarization conversion. After some maths, one arrives at fully analytical expressions for the reflection and transmission coefficients of monolayers of spheres in a homogeneous background as [S6]

$$r_{\rm coh} = \frac{\alpha A_{\rm r}}{1 - \alpha A_{\rm t} + \frac{\alpha^2}{4}\left(A_{\rm t}^2 - A_{\rm r}^2\right)}, \quad t_{\rm coh} = \frac{1 - \frac{\alpha^2}{4}\left(A_{\rm t}^2 - A_{\rm r}^2\right)}{1 - \alpha A_{\rm t} + \frac{\alpha^2}{4}\left(A_{\rm t}^2 - A_{\rm r}^2\right)}. \tag{S7}$$

Here, we have defined $\alpha = \rho 2\pi i / (k_{\rm b}\cos\theta_{\rm i})$, and the forward and backward scattering amplitudes $A_{\rm t} = \hat{\boldsymbol{e}}_{\rm t} \cdot \mathbf{A}(\mathbf{k}_{\rm i}, \mathbf{k}_{\rm i})\hat{\boldsymbol{e}}_{\rm i}$ and $A_{\rm r} = \hat{\boldsymbol{e}}_{\rm r} \cdot \mathbf{A}(\mathbf{k}_{\rm r}, \mathbf{k}_{\rm i})\hat{\boldsymbol{e}}_{\rm i}$ with $\hat{\boldsymbol{e}}_{\rm r}$ and $\hat{\boldsymbol{e}}_{\rm t} \equiv \hat{\boldsymbol{e}}_{\rm i}$ the polarization in reflection and transmission. The expressions in the independent scattering approximation are recovered by expanding Eqs. (S7) in powers of α (i.e., for small densities and near normal incidence), that is, $r_{\rm coh} = \alpha A_{\rm r}$ and $t_{\rm coh} = 1 + \alpha A_{\rm t}$. It is worth noting that the amplitudes of the coefficients in the latter expressions exhibit an unphysical divergence at grazing angles. This shortcoming is completely resolved in Eqs. (S7) [S6]. This will be shown below in the computational results reported in the Supplementary Note 2.

Once the reflection and transmission coefficients for the monolayer in the uniform background are obtained, the impact of a substrate on specular reflectance and transmittance is accounted for via Fresnel equations [S6]. In solving this problem sequentially, one makes the approximation that the interaction between particles via the substrate does not contribute to the average exciting field. The quantitative agreement observed between the model and computational results that will be reported below suggests that this approximation is valid for the metasurfaces considered in this work, even when high-index substrates are considered (Supplementary Figs. 8 and 10). The validity of this sequential approach is likely to degrade for particle-substrate systems exhibiting an efficient coupling between free-space modes and guided photonic or plasmonic modes in the layered substrate.

The specular component of the BRDF can finally be expressed as a function of the reflection coefficient of the particle monolayer on the substrate $r_{\rm st}$ as

$$f_{\rm r}^{\rm spe}(\mathbf{k}_{\rm s}, \hat{\boldsymbol{e}}_{\rm s}, \mathbf{k}_{\rm i}, \hat{\boldsymbol{e}}_{\rm i}) = \frac{\delta(\pi - \theta_{\rm s} - \theta_{\rm i})\delta(\phi_{\rm s} - \phi_{\rm i})\delta_{\hat{\boldsymbol{e}}_{\rm s}, \hat{\boldsymbol{e}}_{\rm i}}}{\sin\theta_{\rm s}\cos\theta_{\rm s}}|r_{\rm st}(\mathbf{k}_{\rm s}, \hat{\boldsymbol{e}}_{\rm s})|^2, \tag{S8}$$

This ensures the specular reflectance efficiency be $\int_{2\pi} f_{\rm r}^{\rm spe}(\mathbf{k}_{\rm i}, \hat{\boldsymbol{e}}_{\rm i}, \mathbf{k}_{\rm s}, \hat{\boldsymbol{e}}_{\rm s})\cos\theta_{\rm s}d\Omega_{\rm s} = |r_{\rm st}(\mathbf{k}_{\rm i}, \hat{\boldsymbol{e}}_{\rm i})|^2$, as expected.

Diffuse reflectance model

The diffuse reflectance of the surface plays a primary role in the present work. State-of-the-art models for the diffuse intensity apply either to (i) particle monolayers suspended in a *homogeneous* background only (this allows the scattered field to be decomposed onto the vector spherical harmonics basis) [S7], or (ii) particles much smaller than

the wavelength on a substrate (this allows using a Green tensor formalism for radiating electric dipoles in layered media) [S8]. Here, we consider particles exhibiting electric and magnetic dipoles and quadrupoles resonances (e.g., Si particles of Fig. 2 in the main text) on substrates. The existing models are thus insufficient for our purpose.

We start by considering the field scattered by an individual particle p on an arbitrary substrate. The far-field scattered upon illumination by an incident planewave reads

$$\mathbf{E}_{\mathrm{s}}^{p}(\mathbf{k}_{\mathrm{s}}, z) = 2\pi i E_{\mathrm{b}} \frac{\exp\left[\pm i k_{\mathrm{s},z} z\right]}{k_{\mathrm{s},z}} \mathbf{A}_{p}(\mathbf{k}_{\mathrm{s}}, \mathbf{k}_{\mathrm{i}}) \hat{e}_{\mathrm{i}} \exp\left[i(\mathbf{k}_{\mathrm{i},\parallel} - \mathbf{k}_{\mathrm{s},\parallel}) \cdot \mathbf{r}_{p,\parallel}\right], \tag{S9}$$

where $\mathbf{k}_{\mathrm{i},\parallel}$ and $\mathbf{k}_{\mathrm{s},\parallel}$ are the projections of the wavevectors of the incident and scattered planewaves on the surface plane and $k_{\mathrm{s},z} = \mathbf{k}_{\mathrm{s}} \cdot \hat{\mathbf{z}} = k_{\mathrm{b}} \cos(\theta_{\mathrm{s}})$ is the projection of the wavevector of the scattered planewave on the surface normal z. Compared to Eq. (S6), the scattering amplitude $\mathbf{A}_{p}$ now takes implicitly into account the interaction between the particle and the substrate. $\mathbf{A}_{p}$ can be computed for particles of any shape in arbitrary layered media with virtually any Maxwell equations solver and a near-to-far-field transformation [S9]. Projecting $\mathbf{E}_{\mathrm{s}}(\mathbf{k}_{\mathrm{s}}, z)$ on an arbitrary polarization $\hat{e}_{\mathrm{s}}$ and taking the absolute square leads to the differential scattering cross-section [S3] of an individual particle p

$$\frac{d\sigma_{\mathrm{s}}^{(1),p}}{d\Omega}(\mathbf{k}_{\mathrm{s}}, \hat{e}_{\mathrm{s}}, \mathbf{k}_{\mathrm{i}}, \hat{e}_{\mathrm{i}}) = \frac{k_{\mathrm{b}}^{2} \cos^{2}(\theta_{\mathrm{s}})}{4\pi^{2}|E_{\mathrm{b}}|^{2}} |\hat{e}_{\mathrm{s}} \cdot \mathbf{E}_{\mathrm{s}}^{p}(\mathbf{k}_{\mathrm{s}}, z)|^{2} = |\hat{e}_{\mathrm{s}} \cdot \mathbf{A}_{p}(\mathbf{k}_{\mathrm{s}}, \mathbf{k}_{\mathrm{i}}) \hat{e}_{\mathrm{i}}|^{2}. \tag{S10}$$

Let us now consider the field scattered by an ensemble of N identical particles distributed on a surface of area S. We will further take the limit $N, S \to \infty$ such that the surface particle density $\rho = N/S$ remains constant. The field scattered by the particle ensemble is $\mathbf{E}_{\mathrm{s}}(\mathbf{k}_{\mathrm{s}}, z) = \sum_{p} \mathbf{E}_{\mathrm{s}}^{p}(\mathbf{k}_{\mathrm{s}}, z)$. In the ISA, one neglects the field scattered by neighboring particles on the exciting field $\mathbf{E}_{\mathrm{exc}}^{p}$ in Eqs. (S1)-(S2), such that one could simply write $\mathbf{A}_{p} \equiv \mathbf{A}$ for identical particles. This approximation however breaks down as soon as the particle density ρ is not vanishingly small and at grazing angles. A more realistic description is obtained by considering that the particles are "dressed" by the interaction with their neighbours. For ensembles of identical particles, it is convenient to define a tensor $\mathbf{c}_{p}$ describing the change in the scattering amplitude of particle p due to the other particles as

$$\mathbf{A}_{p}(\mathbf{k}_{\mathrm{s}}, \mathbf{k}_{\mathrm{i}}) = \mathbf{A}(\mathbf{k}_{\mathrm{s}}, \mathbf{k}_{\mathrm{i}}) \mathbf{c}_{p}(\mathbf{k}_{\mathrm{s}}, \mathbf{k}_{\mathrm{i}}). \tag{S11}$$

The scattering amplitude thus fluctuates from particle to particle due to multiple scattering, the latter being fully described by the unknown tensor $\mathbf{c}_{p}$. To proceed, we write $\mathbf{c}_{p}$ as the sum of its average (upon particle configurations) and a fluctuating part as $\mathbf{c}_{p} = \langle \mathbf{c} \rangle + \delta \mathbf{c}_{p}$, where $\langle \mathbf{c}_{p} \rangle = 0$. To reach an expression for the differential scattering cross-section of the particle ensemble following Eqs. (S4) and (S10), we then assume that the particles are excited by the average (coherent) field, which is quite standard in multiple scattering theory [S1], and take the limit of small fluctuations, $\langle |\delta \mathbf{c}_{p}|^{2} \rangle \ll |\langle \mathbf{c} \rangle|^{2}$, leading to

$$\frac{d\sigma_{\mathrm{s}}}{d\Omega}(\mathbf{k}_{\mathrm{s}}, \hat{e}_{\mathrm{s}}, \mathbf{k}_{\mathrm{i}}, \hat{e}_{\mathrm{i}}) = \frac{k_{\mathrm{b}}^{2} \cos^{2}(\theta_{\mathrm{s}})}{4\pi^{2}|E_{\mathrm{b}}|^{2}} \left(\langle |\hat{e}_{\mathrm{s}} \cdot \mathbf{E}_{\mathrm{s}}(\mathbf{k}_{\mathrm{s}}, z)|^{2} \rangle - |\hat{e}_{\mathrm{s}} \cdot \langle \mathbf{E}_{\mathrm{s}}(\mathbf{k}_{\mathrm{s}}, z) \rangle|^{2} \right),$$

$$= N \frac{d\sigma_{\mathrm{s}}^{(1)}}{d\Omega}(\mathbf{k}_{\mathrm{s}}, \hat{e}_{\mathrm{s}}, \mathbf{k}_{\mathrm{i}}, \hat{e}_{\mathrm{i}}) \mathcal{S}_{\mathrm{r}}(\mathbf{k}_{\mathrm{s},\parallel}, \mathbf{k}_{\mathrm{i},\parallel}) \mathcal{C}(\mathbf{k}_{\mathrm{s}}, \mathbf{k}_{\mathrm{i}}), \tag{S12}$$

with $\mathcal{C} \equiv |\langle \mathbf{c} \rangle|^{2}$. We have also defined the static structure factor $\mathcal{S}_{\mathrm{r}}(\mathbf{k}_{\mathrm{s},\parallel}, \mathbf{k}_{\mathrm{i},\parallel}) \equiv \mathcal{S}(\mathbf{k}_{\mathrm{s},\parallel}, \mathbf{k}_{\mathrm{i},\parallel}) - \rho|\Theta(\mathbf{k}_{\mathrm{s},\parallel} - \mathbf{k}_{\mathrm{i},\parallel})|^{2}/S$ where Θ is the Fourier-transform of a window function equal to 1 in the area occupied by the particles (becoming a Dirac delta function for an infinite surface), and $\mathcal{S}$ is the (two-dimensional) structure factor

$$\mathcal{S}(\mathbf{k}_{\mathrm{s},\parallel}, \mathbf{k}_{\mathrm{i},\parallel}) = \frac{1}{N} \left\langle \sum_{p,q} \exp\left[i(\mathbf{k}_{\mathrm{i},\parallel} - \mathbf{k}_{\mathrm{s},\parallel}) \cdot (\mathbf{r}_{p,\parallel} - \mathbf{r}_{q,\parallel})\right] \right\rangle. \tag{S13}$$

Analytical (or semi-analytical) expressions for the static structure factor can be found in the literature [S10]. Here, we use the Baus-Colot model for two-dimensional, statistically isotropic and translationally-invariant liquids of hard disks [S11].

The diffuse component of the BRDF is finally obtained by normalizing the differential cross-section by the apparent surface $S \cos(\theta_{\mathrm{i}})$ to obtain a scattering efficiency, and by the explicit dependence on the scattering angle $\cos(\theta_{\mathrm{s}})$ [S12], leading to

$$f_{\mathrm{r}}^{\mathrm{dif}}(\mathbf{k}_{\mathrm{s}}, \hat{e}_{\mathrm{s}}, \mathbf{k}_{\mathrm{i}}, \hat{e}_{\mathrm{i}}) = \rho \frac{d\sigma_{\mathrm{s}}^{(1)}}{d\Omega}(\mathbf{k}_{\mathrm{s}}, \hat{e}_{\mathrm{s}}, \mathbf{k}_{\mathrm{i}}, \hat{e}_{\mathrm{i}}) \mathcal{S}_{\mathrm{r}}(\mathbf{k}_{\mathrm{s},\parallel}, \mathbf{k}_{\mathrm{i},\parallel}) \frac{\mathcal{C}(\mathbf{k}_{\mathrm{s}}, \mathbf{k}_{\mathrm{i}})}{\cos(\theta_{\mathrm{i}}) \cos(\theta_{\mathrm{s}})}. \tag{S14}$$

From Eq. (S14), one therefore finds that the BRDF of the metasurface is proportional to the density of particles ρ, the scattering diagram of an individual particle $d\sigma_s^{(1)}/d\Omega$ and the structure factor $\mathcal{S}_r$ to account for a correlations in pairs of particles ($\mathcal{S}_r = 1$ for uncorrelated disorder). The possibility to distinguish between individual and collective effects brings great physical insight for design, which is crucial in our work. These scattering properties are corrected by the function $\mathcal{C}$, which represents a first-order correction to the ISA (wherein $\mathcal{C} = 1$) and describes the modification of the (coherent) exciting field from the incident field due to multiple scattering. It is worth noting that the ISA tends to greatly overestimate the diffuse intensity at grazing angles since both the scattering cross-section $d\sigma_s^{(1)}/d\Omega$ and the structure factor take finite values and the cosines at the denominator diverge.

Obtaining a rigorous expression, or even a numerical estimate, of $\mathcal{C}$ for arbitrary metasurfaces is a notoriously difficult and still unresolved problem, which therefore necessarily relies on approximations. *An important contribution here is to propose a practical, heuristic method to compute an estimate of $\mathcal{C}$ that leads to physically sound and accurate predictions of the diffuse component of the BRDF.* To start, let us note that the specular and diffuse BRDF components must evidently be related with each other, in the sense that an increase (resp., decrease) of the specular reflectance must be accompanied by a decrease (resp., an increase) of the diffuse reflectance. Assuming as above that the particles are excited by a planewave with a modified amplitude to account for multiple scattering effects, we can establish a relation between the specular and diffuse components, as

$$1 - T_{st}(\theta_i, \hat{e}_i) - R_{st}(\theta_i, \hat{e}_i) = \frac{\rho\sigma_e(\theta_i, \hat{e}_i)}{\cos(\theta_i)}\gamma(\theta_i, \hat{e}_i). \tag{S15}$$

We generalize here an expression that was derived in Ref. [S8] in the case of point dipole scatterers. T_{st} and R_{st} are the specular transmittance and reflectance through the monolayer of particles on the layered substrate, evaluated from Eq. (S7), σ_e is the extinction cross-section of an individual particle on the layered substrate and γ describes the variation of the intensity exciting the particle due to the presence of neighboring particles. The left-hand side of Eq. (S15) thus describes the extinction from the particle monolayer by removing the specular reflectance and transmittance, and the right-hand side describes the extinction expected from an assembly of particles whose excitation is modified by a coefficient γ.

In practice, T_{st} and R_{st} are obtained from the multiple-scattering model presented in the previous section, ρ is an input parameter and σ_e is computed using fully-vectorial Maxwell's equations solvers. We can thus compute the excitation coefficient γ for all angles θ_i and both s and p polarizations.

The coefficients $\mathcal{C}$ in Eq. (S14) and γ in Eq. (S15) are evidently related to each other. On phenomenological arguments, we propose to define the correction coefficient as the harmonic mean of the excitation coefficients γ for the incident and scattered planewaves, that is

$$\mathcal{C}(\theta_s, \hat{e}_s, \theta_i, \hat{e}_i)^{-1} = \frac{1}{2}\left(\gamma(\theta_i, \hat{e}_i)^{-1} + \gamma(\theta_s, \hat{e}_s)^{-1}\right). \tag{S16}$$

This ensures that the diffuse component of the BRDF behaves correctly in all situations. For instance, a dominant specular behavior is expected at increasing particle densities and/or at grazing angles of incidence. This will result in a small excitation coefficient $\gamma(\theta_i)$, leading to a suppression of the diffuse term. Similarly, the diffuse intensity is expected to be weak at grazing scattering angles. This behavior will be obtained via a small excitation coefficient $\gamma(\theta_s)$. Finally, at low particle densities and near normal incident and scattering angles, the excitation coefficients γ approach one, leading to a correction coefficient $\mathcal{C} \approx 1$, such that Eq. (S14) naturally tends to the rigorous expression obtained within the ISA, as expected.

Although our model for the diffuse component of the BRDF is most likely unable to provide quantitative predictions for arbitrary metasurfaces, it is physically sound and intuitive, and it yields very satisfactory predictions for the broad panel of metasurfaces already considered in the present study, as will be confirmed by comparisons with full-wave computations in the next section.

SUPPLEMENTARY NOTE 2. VALIDATION OF THE BRDF MODEL WITH FULL-WAVE MULTIPLE-SCATTERING COMPUTATIONS

To test the accuracy of our approximate BRDF model, we perform full-wave computations of the scattering by disordered metasurfaces, taking all multiple scattering phenomena into account rigorously. The method, which is presently developed by some of us [S13, S14], relies on the concept of a global polarizability matrix to handle possibly dense systems composed of hundreds of particles in interaction in layered media. It can model particles exhibiting high-order multipolar resonances (i.e., beyond the electric dipole) and use either open or periodic boundary conditions. The method is expected to provide accurate quantitative predictions of the specular and diffuse reflectances and of the scattering diagram, except at grazing incident and scattering angles due to the finiteness of the system. Indeed, full-wave simulations can only handle finite number of particles (making up systems of a few wavelengths squared), which is not necessarily representative of macroscopic surfaces in terms of scattering. We tackle this issue by combining two approaches.

First, we estimate the average specular and diffuse reflectances integrated over the upper hemisphere by using a supercell approach, i.e., by computing the power radiated into the diffraction orders of a periodic system whose unit cell contains a large number of particles. Indeed, as the size of the supercell increases, the discrete spectrum of diffracted orders is expected to become a faithful approximation of the (continuous) radiation diagram of the infinite surface. Then, the $(0,0)$th diffraction order efficiency tends towards the specular reflectance, and the sum of all other diffraction-order efficiencies tends toward the diffuse reflectance. As shown below, we have checked that the average response converges towards stabilized values, which may then be considered as exact statistical predictions of the infinite, translationally-invariant surface.

Second, to estimate the diffuse scattering diagram, we consider a finite-size system as large as possible, compute the radiation diagram by solving Maxwell's equations and average over independent realizations to obtain the fluctuating field ($\langle|\delta\mathbf{E}|^2\rangle = \langle|\mathbf{E}|^2\rangle - |\langle\mathbf{E}\rangle|^2$). Due to the finite size of the considered system, the predictions are necessarily incorrect at grazing incident and scattering angles. Indeed, while diffuse scattering by infinitely large surfaces should vanish as θ approaches $\pi/2$, it does not for finite-size surfaces. Nevertheless, these calculations provide a quantitative prediction of the radiation diagram for illumination and viewing directions reasonably different from 90°, from which the predictive force of the model can be tested.
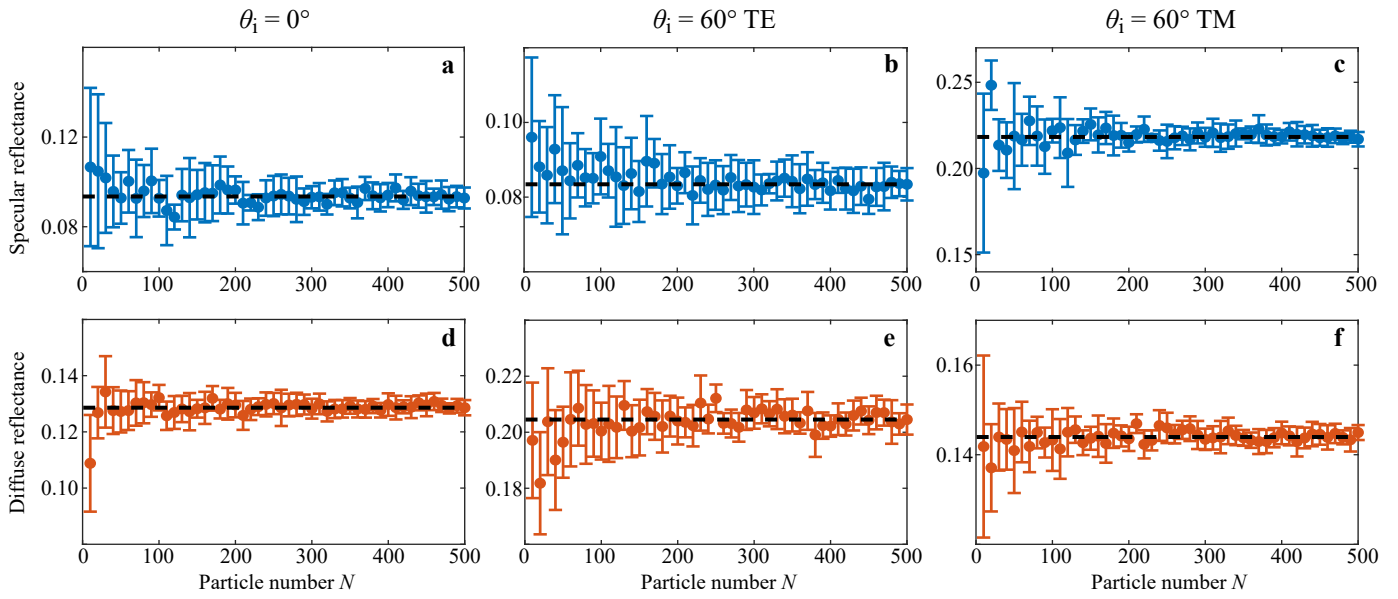
Convergence study with the supercell method

The simulations using the supercell approach are made for two particles: Silicon (Si) particles of radius $r = 70$ nm (similar to the particles considered in Fig. 2 of the main text), and Silver (Ag) particles of radius $r = 90$ nm, identical to those considered in Figs. 1, 3 and 4 of the main text.

We start by checking the convergence of the supercell approach with increasing number of particles N. Results are reported in Supplementary Figs. 1 to 6. Simulations are performed for a set of three incident angles and polarisations ($\theta_i = 0°$, 60° for TE polarisation, 60° for TM polarisation) and two wavelengths ($\lambda = 580$ nm and 440 nm). The results are averaged over 10 disorder realisations, and the error bars correspond to the standard deviation.

We first consider monolayers of particles in air. Each particle is described by electric and magnetic dipoles. This allows us to simulate large ensembles of particles (up to $N = 500$) and investigate the asymptotic convergence of the supercell method with a reasonably low computational load. The results are presented in Supplementary Figs. 1-3. For all computations, we observe a stabilization of the average towards a constant value and a decrease of the standard deviation with increasing N. Convergence appears to be obtained. Interestingly, it appears that the asymptotic value can be already estimated with good accuracy for systems containing a few tens of particles.

As a second step, we consider the more realistic case of particles on a substrate (thereby using the Green tensor of a stratified medium in the computations) and incorporate electric and magnetic quadrupolar terms in the scattering properties of the each particle. We consider here a smaller range of particle number N (due to heavier computational load). The results are presented in Supplementary Figs. 4-6, where we observe a good convergence already for $N \gtrsim 40$. Based on this, we choose $N = 50$ for the following tests to obtain a good balance between convergence accuracy (with confidence interval of about 0.02 in absolute value) and computational time (on the order of 10 minutes per wavelength for particles on substrates).
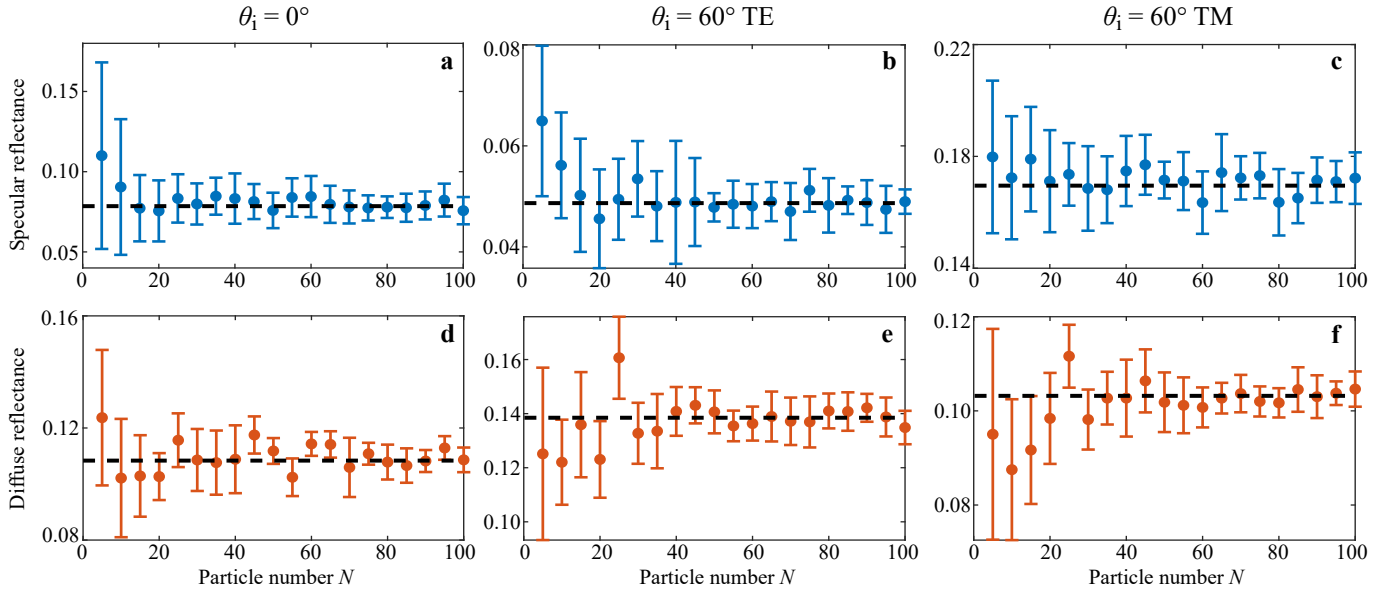
Supplementary Figure 1: Convergence test of the supercell method for the specular and diffuse reflectance spectra. Reflectance takes values between 0 and 1. The reported values and the error bars are the average values and the standard deviations obtained upon 10 disorder realizations. The black dashed lines serve as guides to the eye. The system is a statistically uniform monolayer of spherical Si particles with radius $r = 70$ nm in air at a surface coverage $f = 0.1$ and correlation parameter $p = 0.1$. The wavelength is $\lambda = 580$ nm.
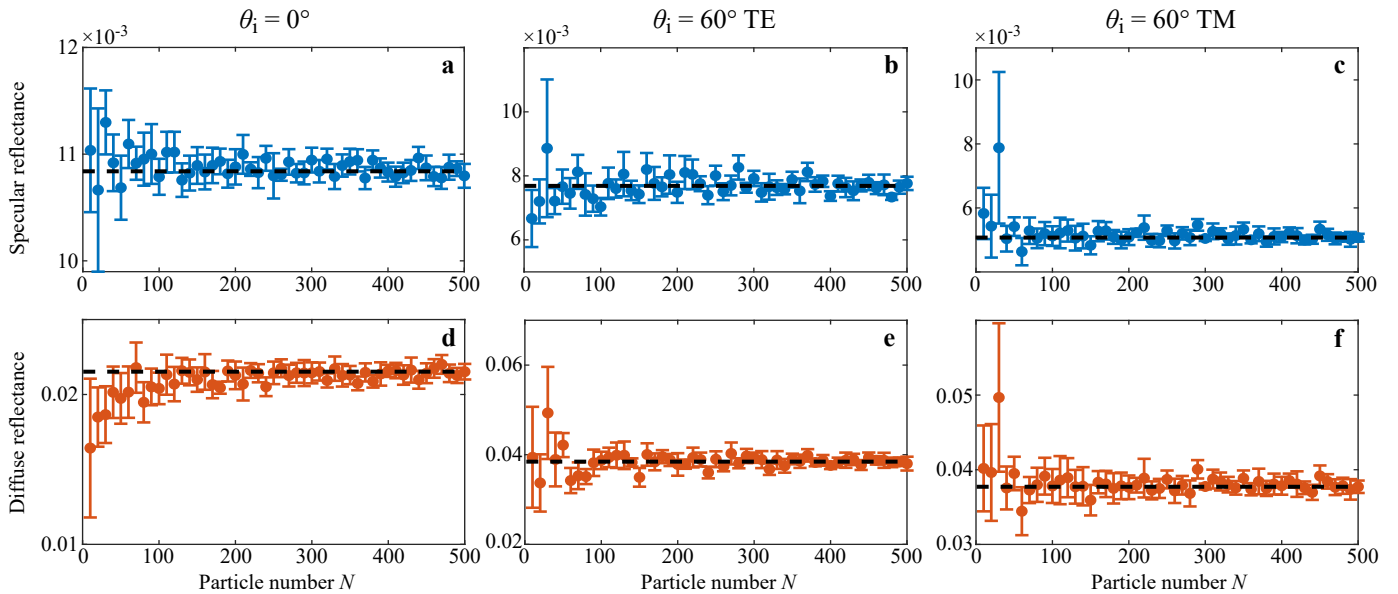
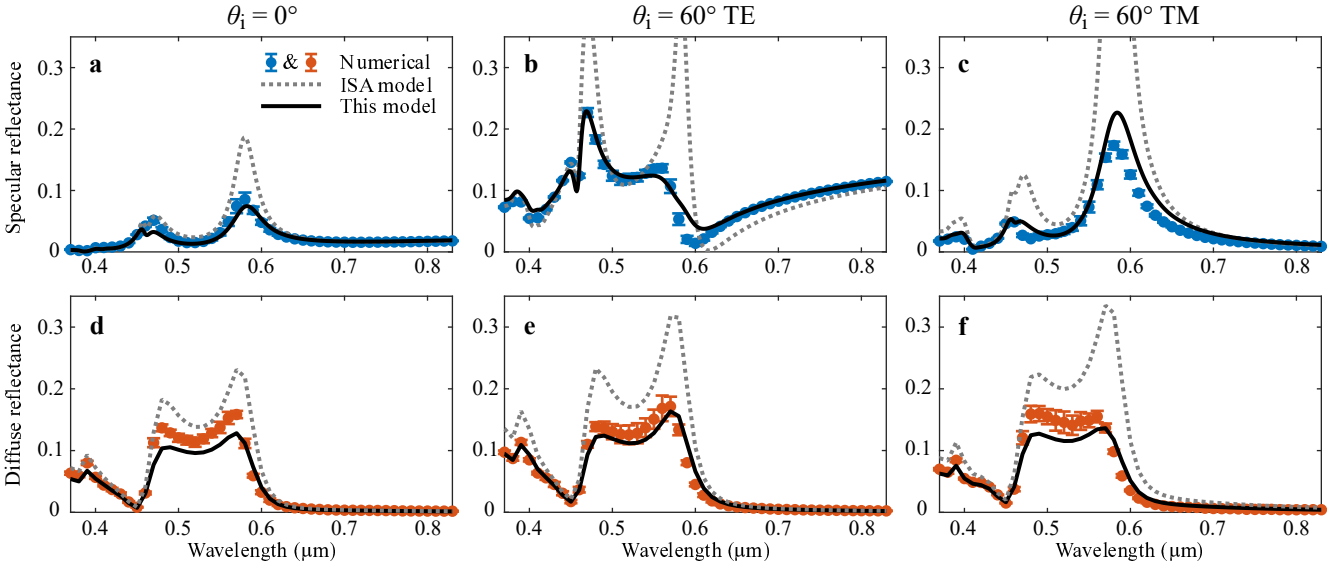**Supplementary Figure 2:** Same as Supplementary Fig. 1 for a wavelength $\lambda = 440$ nm.
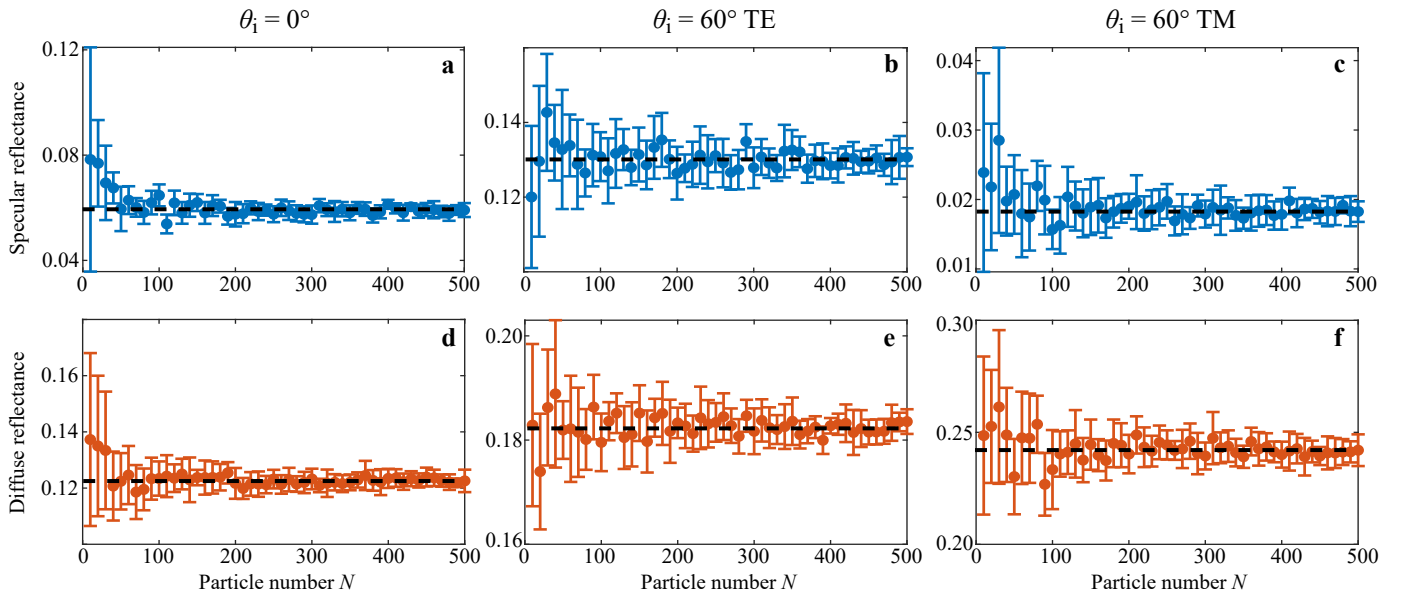
Supplementary Figure 3: Same as Supplementary Fig. 1 for spherical Ag particles of radius $r = 90$ nm.

Supplementary Figure 4: Convergence test of the supercell method for particles *on substrate*. A smaller range of N is considered here, compared to Supplementary Figs. 1-3. The system is a statistically uniform monolayer of spherical Si particles with radius $r = 70$ nm on a glass substrate at a surface coverage $f = 0.1$ and correlation parameter $p = 0.1$. The wavelength is $\lambda = 580$ nm.
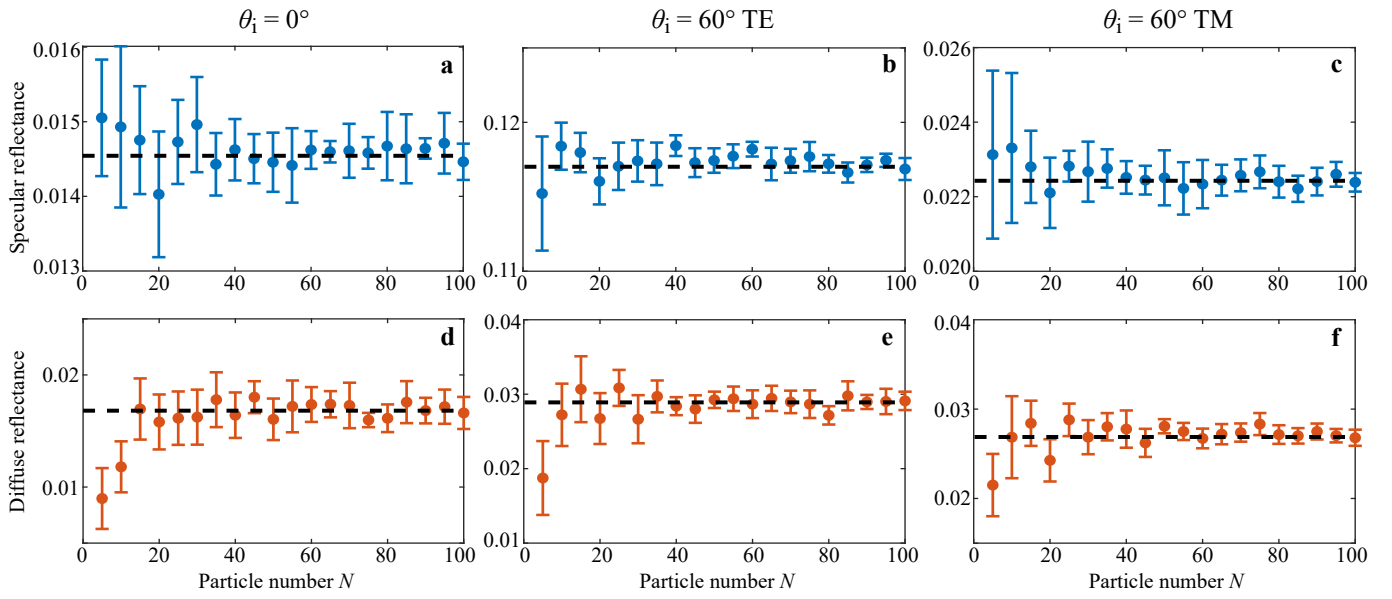
Supplementary Figure 5: Same as Supplementary Fig. 4 for a wavelength $\lambda = 440$ nm.
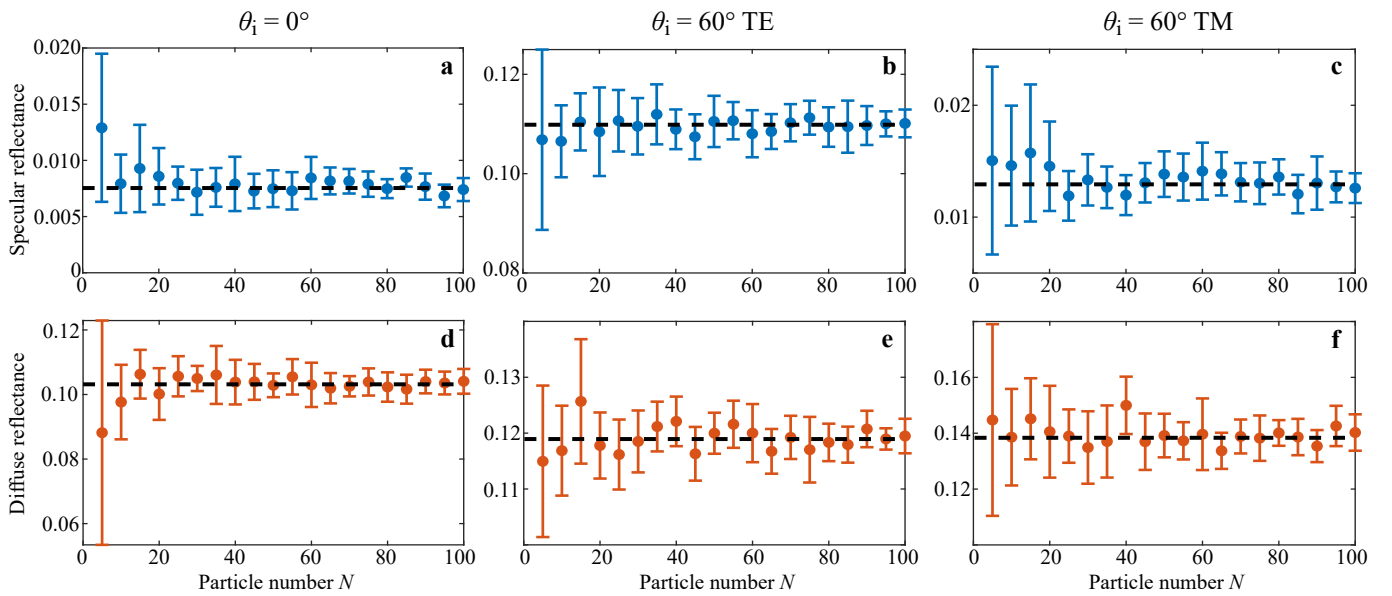
Supplementary Figure 6: Same as Supplementary Fig. 4 for spherical Ag particles of radius $r = 90$ nm.

**Comparison between model predictions and full-wave computational results with the supercell method**

Supplementary Figures 7, 8, 9 and 10 show the specular and diffuse reflectance spectra over the range considered for the predictions reported in the main text, for Si and Ag particles on either a glass substrate or a layered SiO_2/Si substrate with $h = 400$ nm, respectively. The numerical results are compared with the predictions of the BRDF model to test its accuracy. We also add the predictions obtained with the independent scattering approximation (ISA) to highlight the benefit of our model. As explained above, the ISA model is expected to largely overestimate the reflectance (both specular and diffuse) by the surface, especially at grazing angles. This expectation is confirmed by our simulations. By comparison, keeping in mind a confidency interval of about 0.02 on the numerical results, the BRDF model for the specular reflectance [S6] nicely agrees with the numerics in most cases, with only a small overestimate in some cases (e.g., at 60° in TM-polarization), while our heuristic model for the diffuse reflectance generally tends to slightly underestimate it. Nevertheless, the predicted reflectances remain accurate even at large angles of incidence and the important spectral features that play a major role in the produced appearances are accurately reproduced in all cases. The former avoids the unphysical predictions of the ISA model for which the surface would "generate" energy and the latter gives us great confidence in the capability of our approach to synthetise realistic images of various objects covered of disordered metasurfaces.

To be more quantitative on the benefit of our BRDF model compared to the ISA, we compute the colour difference ΔE between predictions from the models and the full-wave supercell computations. ΔE is a real-valued positive quantity that aims at quantifying the colour difference as perceived by the human eye; a $\Delta E \leqslant 1$ is generally considered as an imperceptible colour difference, which becomes perceptible at a glance (yet without being strikingly different) up to about 10. These numbers should however be taken with caution as the perception of colour difference is a complex psychophysical process that varies with the observer, the object and the observation conditions, and various ΔE models yielding quantitatively different results have been developed over the years [S15]. Here, the calculation of ΔE is based on the CIE2000 standard with illuminant E (equal weigth to all wavelengths), taking the spectra shown in Supplementary Figs. 7-10 as inputs. Results are displayed in the Supplementary Tables I-IV. When analysing these numbers, one should also keep in mind that the colour predicted for the diffuse reflectance is *not* the colour that would be observed under a certain viewing angle due to the integration over the upper hemisphere. With a ΔE on the order of 5 on average and slightly above 10 at the highest, our model incorporating multiple scattering leads to better predictions than the ISA on both specular and diffuse reflectances in general (23 situations out of 24), often reducing the ΔE by a factor of 2 or more. Note that the ISA can reach very large values of ΔE (up to about 50 in our tests) at oblique incidence, clearly showing that the ISA model should not be used for BRDF predictions.

All in all, these comparisons make us very confident about the specular and diffuse colours predicted for particles laying on both homogeneous and layered substrates in Figs. 1, 2 and 3 of the main text.

Supplementary Figure 7: Comparison between the model predictions models and numerical data obtained with the supercell approach for the specular and diffuse reflectance spectra of a monolayer of spherical silicon particles with radius $r = 70$ nm deposited on a glass substrate with a filling fraction $f = 0.1$ and correlation parameter $p = 0.1$. All spectra share the same vertical axis for better comparison.
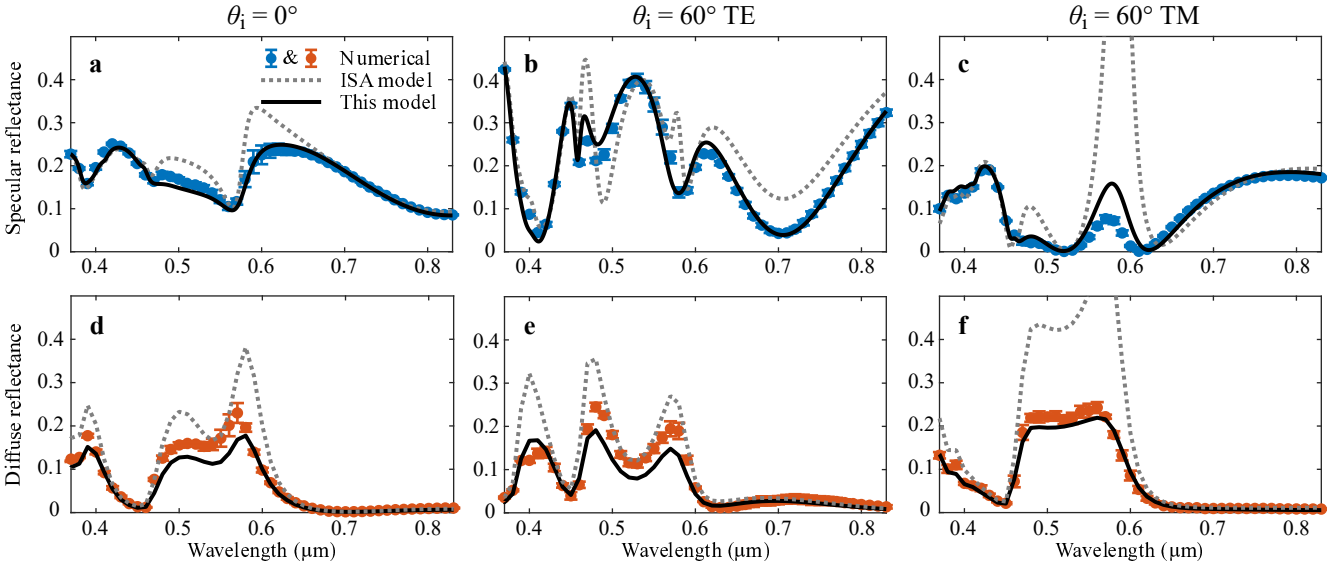
Supplementary Figure 8: Same as Supplementary Fig. 7 for a SiO_2/Si substrate with a thickness $h = 400nm$.
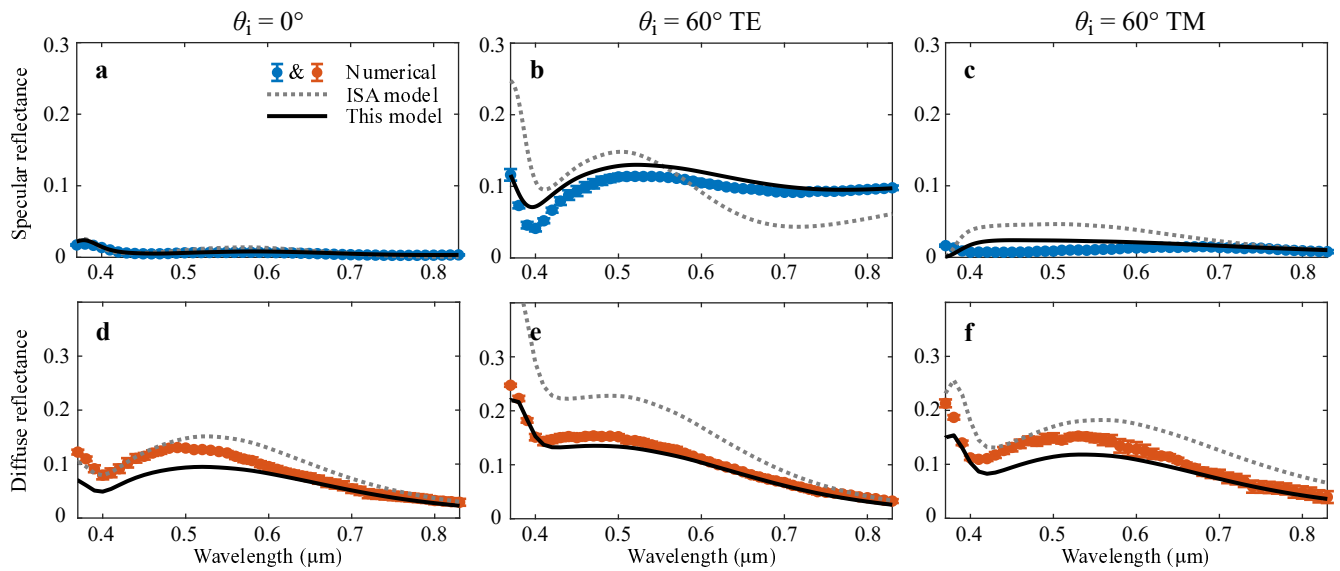
Supplementary Figure 9: Same as Supplementary Fig. 7 for spherical silver particles with radius $r = 90$ nm.
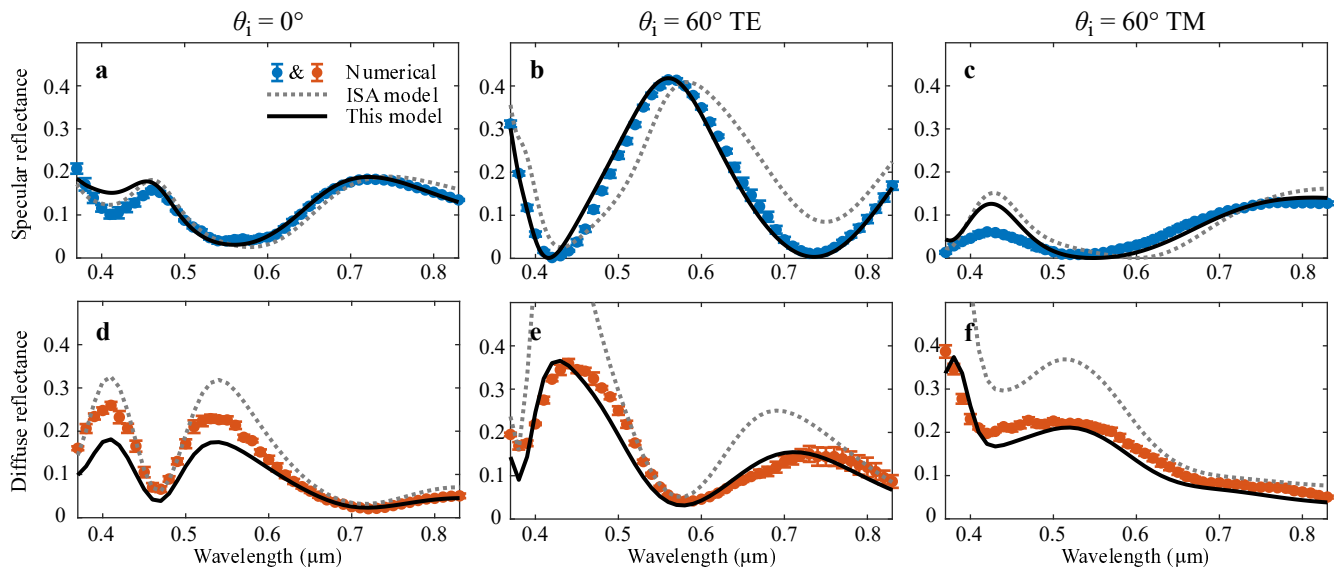
Supplementary Figure 10: Same as Supplementary Fig. 9 for a SiO$_2$/Si substrate with a thickness $h = 400nm$.

	0°		60° TE		60° TM	
	ΔE_{ISA}	ΔE_{MS}	ΔE_{ISA}	ΔE_{MS}	ΔE_{ISA}	ΔE_{MS}
Specular refl.	10.62	4.43	11.96	2.67	27.64	6.30
Diffuse refl. (integrated)	6.01	3.10	9.62	3.75	13.10	3.59

Supplementary Table I: Colour difference between predictions from either the ISA model (ΔE_{ISA}) or the present multiple-scattering model (ΔE_{MS}) and full-wave supercell computations. The calculation of ΔE is based on the CIE2000 standard with illuminant E (equal weigth to all wavelengths) for the metasurface considered in Supplementary Fig. 7 (Si particles on a glass substrate).

	0°		60° TE		60° TM	
	ΔE_{ISA}	ΔE_{MS}	ΔE_{ISA}	ΔE_{MS}	ΔE_{ISA}	ΔE_{MS}
Specular refl.	7.77	2.82	7.90	1.70	53.72	11.07
Diffuse refl. (integrated)	8.96	5.27	6.68	8.46	18.89	2.26

Supplementary Table II: Same as Supplementary Table I for the metasurface considered in Supplementary Fig. 8 (Si particles on a SiO_2/Si substrate).

	0°		60° TE		60° TM	
	ΔE_{ISA}	ΔE_{MS}	ΔE_{ISA}	ΔE_{MS}	ΔE_{ISA}	ΔE_{MS}
Specular refl.	5.43	1.11	10.29	2.59	13.93	8.60
Diffuse refl. (integrated)	5.89	5.55	8.79	2.11	6.70	4.83

Supplementary Table III: Same as Supplementary Table I for the metasurface considered in Supplementary Fig. 9 (Ag particles on a glass substrate).

	0°		60° TE		60° TM	
	ΔE_{ISA}	ΔE_{MS}	ΔE_{ISA}	ΔE_{MS}	ΔE_{ISA}	ΔE_{MS}
Specular refl.	6.03	4.53	11.23	4.47	15.81	10.74
Diffuse refl. (integrated)	7.84	6.38	13.37	8.30	11.43	4.86

Supplementary Table IV: Same as Supplementary Table I for the metasurface considered in Supplementary Fig. 10 (Ag particles on a SiO_2/Si substrate).

Validation of scattering diagrams for uncorrelated and correlated disorder with finite-size computations

The simulations for finite-size systems are performed for monolayers of either Si or Ag particles in air at a fixed density of $\rho = 2.5 \ \mu m^{-2}$ ($f = 0.039$ and $f = 0.064$, respectively). Results are shown in Supplementary Figs. 11 and 12 for an incident planewave ($\theta_i = 30°$ TE-polarisation) at two wavelengths ($\lambda = 440$ nm and 580 nm), and two correlation degrees, $p = 0.1$ and $p = 0.5$. The results are obtained for 500 independent disorder realizations (needed to smooth out the speckle pattern) of ensembles of 200 particles, which therefore requires significant computational time. Recalling that the full-wave computational results are expected to be inaccurate for grazing scattered angles, we observe a striking similarity on the impact of structural correlations on scattering. While the structures with $p = 0.1$ scatter light with no strong preferential direction, the sharp angular features due to structural correlations are nicely reproduced for the structures with $p = 0.5$.

This agreement between two largely different approaches makes us very confident that the visual effects predicted in Figs. 1 and 4 in the main text for correlated disorders are indeed real. Even more convincing are the experiments on centimetre-scale samples, reported in Fig. 5 of the main text, the Supplementary Note 5 below, and the Supplementary Video 3, which clearly show the impact of short-range structural correlations on light scattering and visual appearance.

BRDF model   Numerical
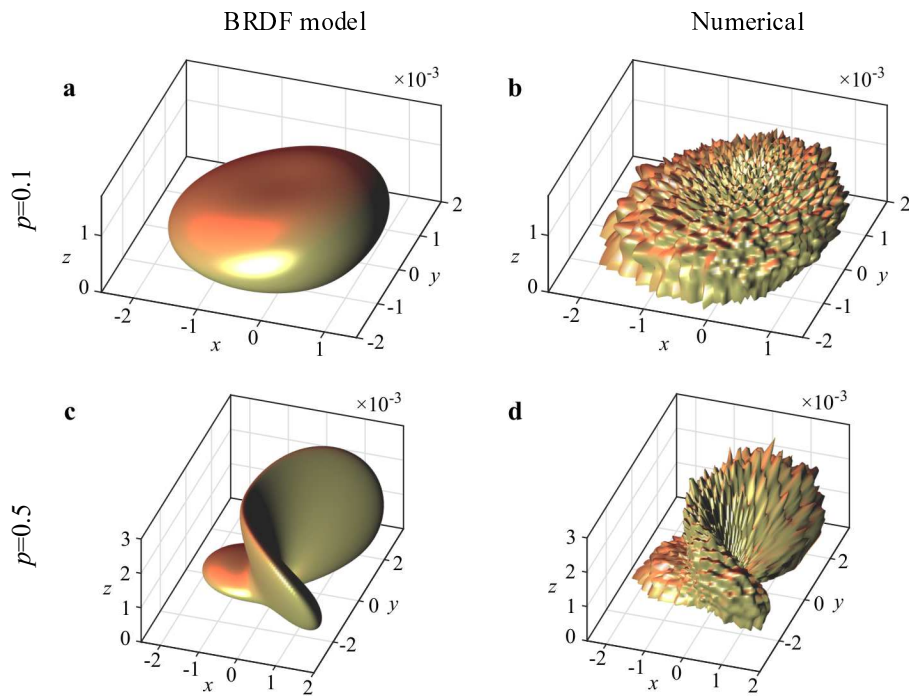
Supplementary Figure 11: Scattering diagrams of the diffuse intensity from the BRDF model (left) and from full-wave computations for finite-size systems (right), for monolayer of Si particles with radius $r = 70$ nm in air at a particle density $\rho = 2.5\ \mu m^{-2}$ and correlation parameters $p = 0.1$ and $p = 0.5$, illuminated by a TE-polarised planewave with wavelength $\lambda = 440$ nm and incident angle 30°. Note the inaccuracy of the numerical data at grazing scattered angles, explained by finite-size effects. The BRDF model does not suffer from this limitation.

BRDF model   Numerical
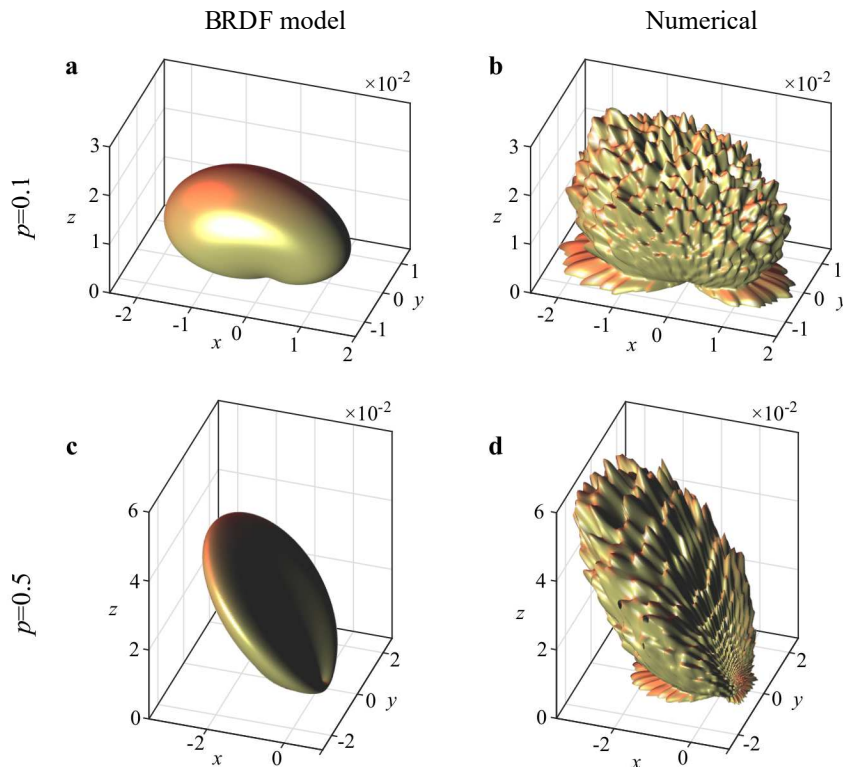
Supplementary Figure 12: Same as Supplementary Fig. 11 for Ag particles with radius $r = 90$ nm at $\lambda = 580$ nm.

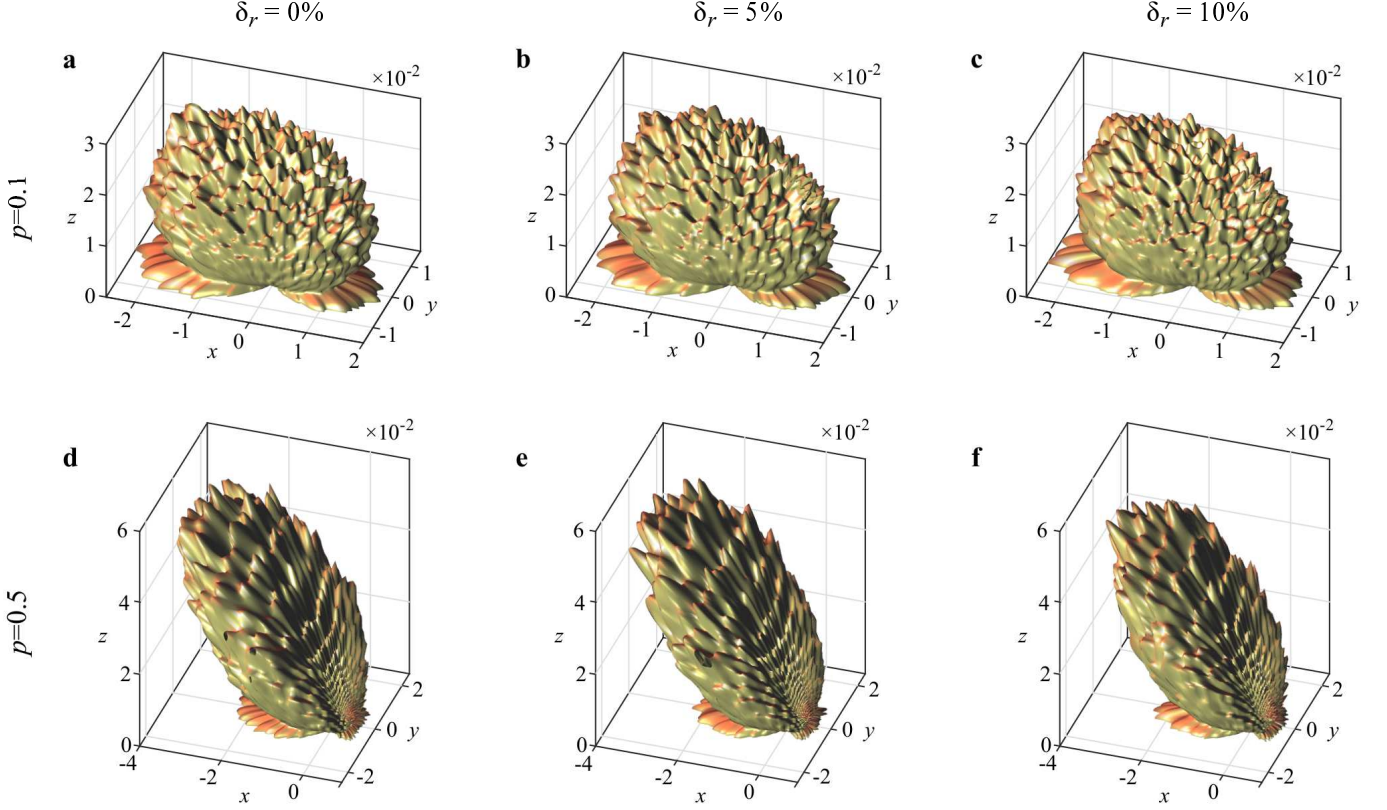# SUPPLEMENTARY NOTE 3. TOLERANCE TO PARTICLE POLYDISPERSITY

Bottom-up nanofabrication is a promising approach for the deployment of large-scale disordered metasurfaces in visual appearance design. However, one has to deal with polydispersity in particle size, that is generally of the order of 10 %. To evaluate the robustness of the scattering properties of the metasurfaces to polydispersity, we perform rigorous full-wave computations similar to those of the previous section, i.e. taking all interactions between particles and interfaces into account. We generate configurations of particles of radii given by a normal distribution with mean r and standard deviation σ_r. The ratio $\delta_r = \sigma_r/r$ determines the degree of polydispersity.

Let us start by testing the diffuse iridescence with a monolayer of Ag particles on top of a layered, SiO_2/Si substrate with $h = 400$ nm. The Supplementary Fig. 13 shows the specular and diffuse reflectance spectra, computed with the supercell method, for the monodisperse system (blue and red markers) and for the polydisperse system (black markers) with a polydispersity $\delta_r = 10\%$. Quite remarkably, the spectra are almost unaffected by polydispersity. This can be explained by considering that the observed spectral and angular features stem essentially from the interference between the field scattered by the particle and the field multiply-reflected in the layer, and not from the (spectrally-broad) optical resonances of the individual Ag particles. This further indicates that the diffuse iridescence shown in Fig. 3 of the main text would persist even for a polydispersity of (at least) $\delta_r = 10\%$ in size.
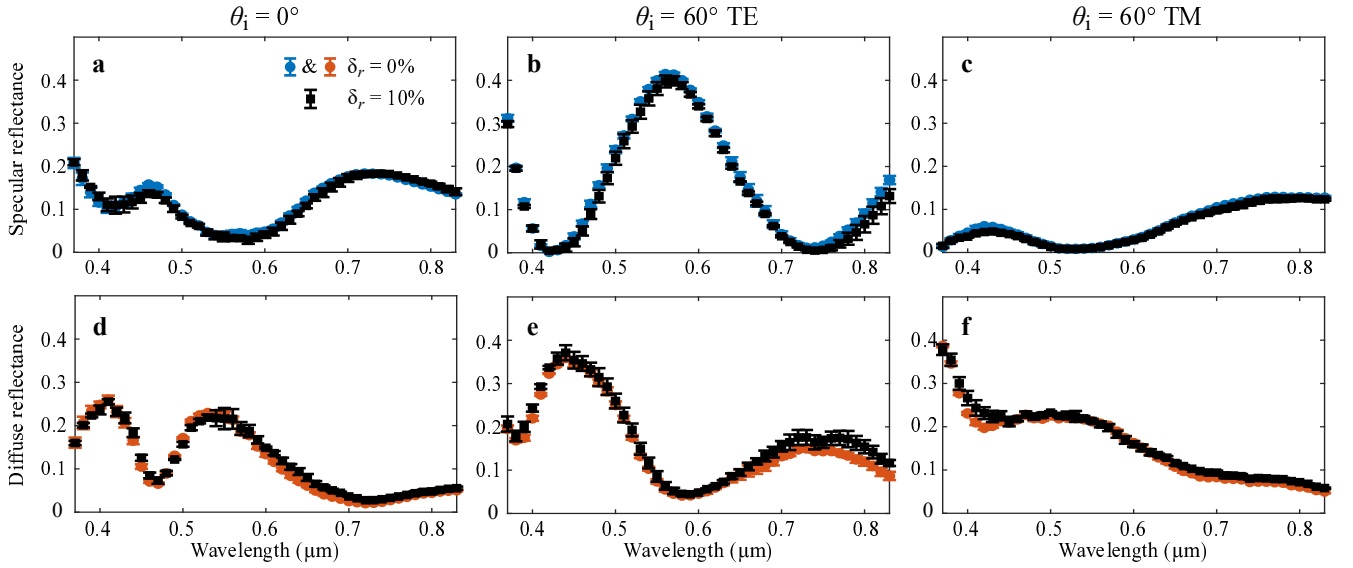

Supplementary Figure 13: Tolerance of specular and diffuse reflectance spectra on particle polydispersity for a monolayer of Ag particles with average radius $r = 90$ nm deposited on a SiO_2/Si substrate with $h = 400$ nm at a filling fraction $f = 0.1$ and correlation parameter $p = 0.1$. This system leads to the "diffuse iridescence" effect reported in Fig. 3 of the main text. The blue and red markers show the spectra for the monodisperse system (already shown in Supplementary Fig. 10) and the black square markers those for the polydisperse system with a particle size polydispersity $\delta_r = 10\%$. Polydispersity has a negligible effect on the spectral features.

The same conclusion is reached for the diffuse halo shown in Fig. 4 of the main text and obtained for a monolayer of Ag particles with a short-range correlation. The Supplementary Fig. 14 shows the scattering diagrams of the diffuse intensity for weakly correlated ($p = 0.1$) and strongly correlated ($p = 0.5$) systems for $\delta_r = 0$, 5 and 10 %. The angular distribution and amplitude of the scattered light are basically unaffected by polydispersity, because the scattering properties of the Ag particles vary weakly on average with the particle size fluctuations, and the modification of the scattering diagram due to short-range correlations is due to the structure factor only, which is independent of the particle size. The diffuse halo shown in Fig. 4 of the main text will thus withstand polydispersity up to at least $\delta_r = 10\%$.


Supplementary Figure 14: Tolerance of the scattering diagrams of the diffuse intensity on particle polydispersity for a monolayer of Ag particles with average radius $r = 90$ nm in air at a particle density $\rho = 2.5\ \mu m^{-2}$ and correlation parameters $p = 0.1$ and $p = 0.5$, illuminated by a TE-polarised planewave with wavelength $\lambda = 580$ nm and incident angle $30°$. The particle size polydispersity δ_r goes from 0 to 10 %. The effect of polydispersity up to $\delta_r = 10\%$ is negligible.

The weak sensitivity to size polydispersity is helped by the fact that the optical response of individual Ag particles (or equivalently, the induced dipole moments) varies relatively weakly with small size variations. This contrasts with high-index dielectric particles exhibiting spectrally sharp Mie resonances as illustrated in Fig. 2 of the main text. To illustrate this, we compute the specular and diffuse reflectance spectra of a disordered metasurface made of Si particles with average radius $r = 70$ nm on a glass substrate with a polydispersity $\delta_r = 10\%$. As shown in Supplementary Fig. 15, the resonances are smoothed out with a weaker amplitude and a broader linewidth. This would lead to a reduced glossiness and fainted diffuse colours. Note that this conclusion applies to all dielectric metasurfaces considered in the literature for applications in structural colouration.
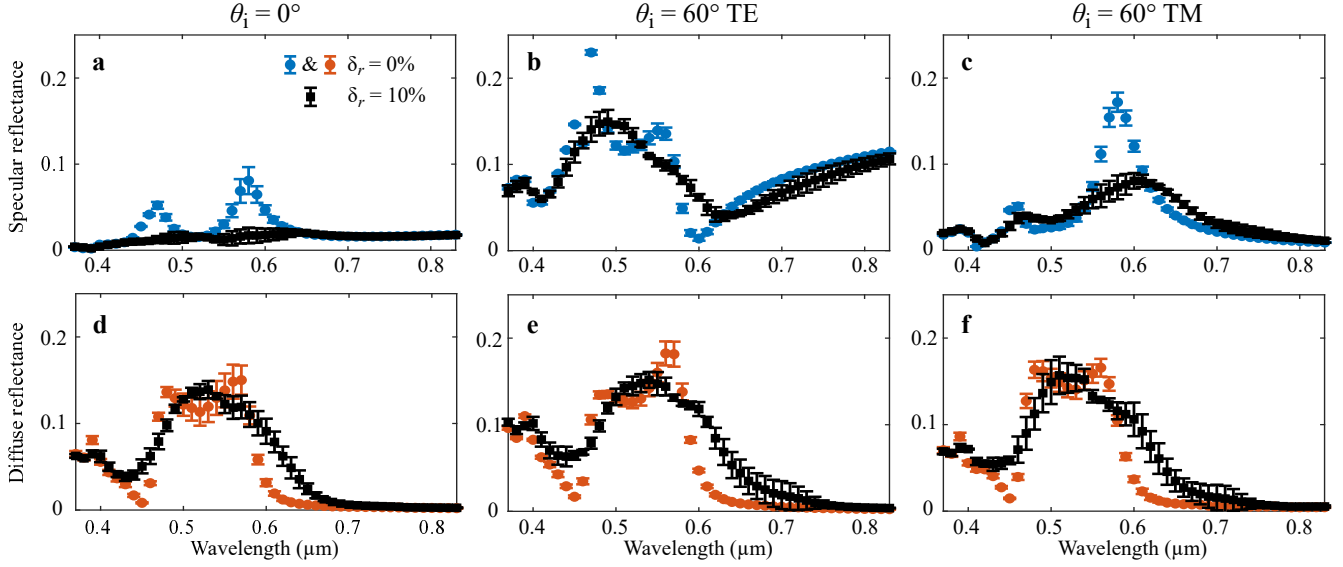
Supplementary Figure 15: Same as Supplementary Fig. 13 for Si particles with average radius $r = 70$ nm on a glass substrate. The impact of polydispersity is stronger here due to Mie resonances that spectrally broaden with particle size variations.

A less obvious question is whether the exotic visual effects coming from mesoscale interference resist polydispersity. A first answer is provided in Supplementary Fig. 16, where we compute the scattering diagrams of disordered metasurfaces made of Si particles for weak ($p = 0.1$) and strong ($p = 0.5$) short-range structural correlations. The variation of the scattering amplitude (here at $\lambda = 440$ nm) with polydispersity is fully explained by the spectral broadening effect described above. More importantly for us, short-range structural correlations still lead to a significant modification of the scattering diagram for the diffuse intensity with a reduction of the intensity around the specular direction and an enhancement at larger angles. This indicates that the diffuse halo with dielectric metasurfaces, as demonstrated experimentally in our work (Fig. 5 of the main text), would persist even for a size polydispersity of about 10%.
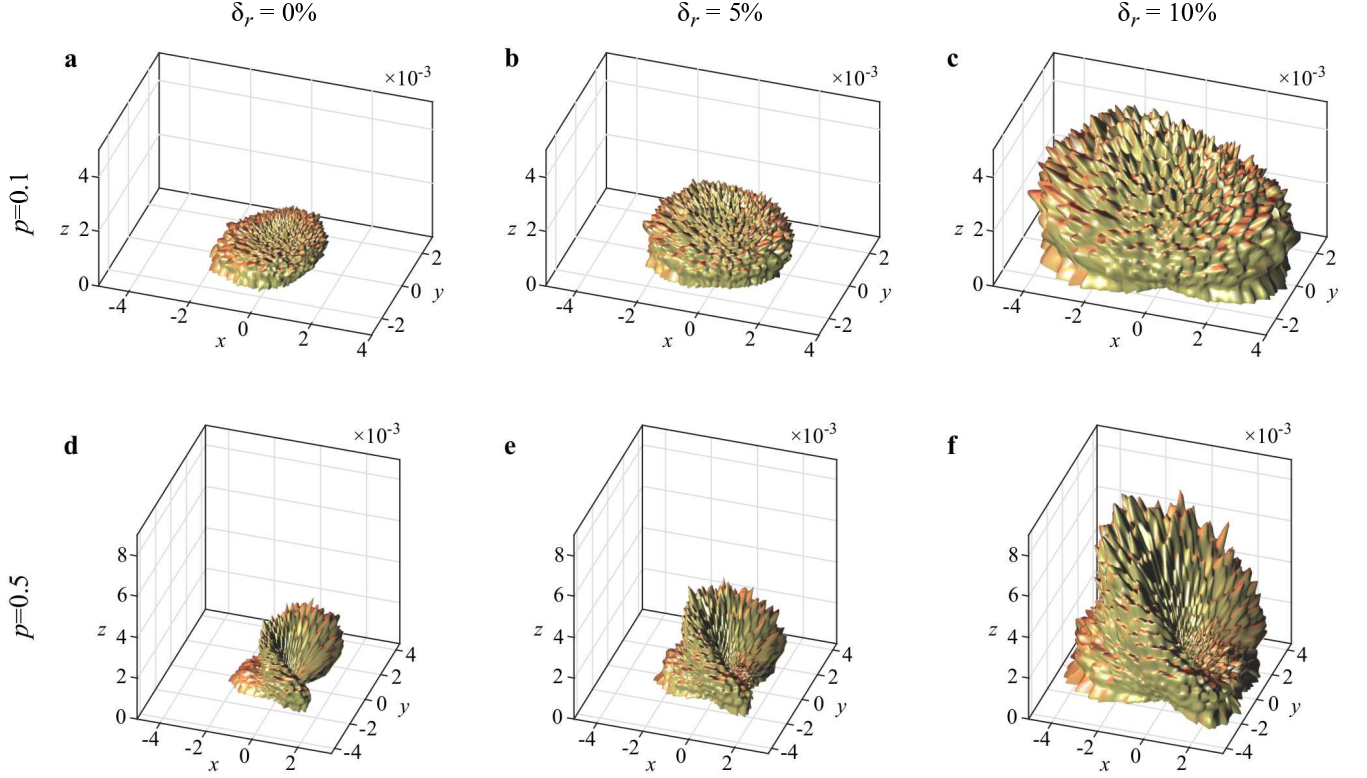
Supplementary Figure 16: Same as Supplementary Fig. 14 for Si particles with average radius $r = 70$ nm at $\lambda = 440$ nm. The suppression of the diffuse intensity near the specular direction due to structural correlations remains clearly visible.

SUPPLEMENTARY NOTE 4. VALIDATION OF THE RENDERED IMAGES

The comparison of the BRDF model predictions with full-wave multiple-scattering computations presented in the Supplementary Note 2 ensures that the reflectance properties of the disordered metasurface are predicted with good quantitative agreement. Here, we proceed with the validation of the visual appearance of macroscopic objects covered by a disordered metasurface. The rendering technique used in this work on the spherical probe and speedshape objects, as described in the Methods, is said to be predictive. Indeed, given a surface with macroscopic deformations (i.e., having curvature radii much larger than the wavelength), characterized by specific reflectance properties and light sources with specific positions, directions and spectra, the light propagation between the source, the surface and the observer can be considered as exact. We do not discuss here the approximation due to the use of environment maps for outdoor environments. Thus, beyond the actual predictive capability of the BRDF model, the main approximations on the appearance predictions made here may be categorized as follows.

The first approximation concerns the applicability of a BRDF model in general. Indeed, a real material may be partly transparent and exhibit subsurface scattering, in which case light can exit the medium at a point from the surface that differs from the entry point. In the present work, we assumed that light impinging on the surface at a point does not "spread" on macroscopic distances in the monolayer to exit at another point, which is very reasonable. We further assumed that light scattered in transmission through the monolayer of particles on substrate is lost by absorption for all wavelengths. This is the case of the Si substrates considered in Figs. 1 and 3 of the main text, and is also realistic for tinted glass substrate used in Figs. 1, 2 and 4.

The second approximation concerns the discretization of the BRDF, which stems from the fact that the scattering properties of the particles are computed numerically. As described in the Methods, the BRDF is discretized in the wavelengths with a 10 nm resolution, and in the incident and scattering angles with 0.5° and 1° resolutions for the zenith and azimuth angles. To verify that the considered resolutions are sufficient, we compute the BRDF of a disordered metasurface producing strong spectral and angular variations due to both a layered substrate and structural correlations, with different spectral and angular resolutions, and compared the resulting rendered images. Results are shown in Supplementary Fig. 17 for the spectral resolution, and in Supplementary Fig. 18 for the angular resolution. One can hardly distinguish any difference by eye in the various appearance features.

Thus, the rendered images shown in this work do not suffer from spectral or angular discretisation and are representative of the visual appearances that would be observed in reality given the BRDF of the disordered metasurfaces and the lighting environment.

$\Delta\lambda$=2 nm $\Delta\lambda$=10 nm
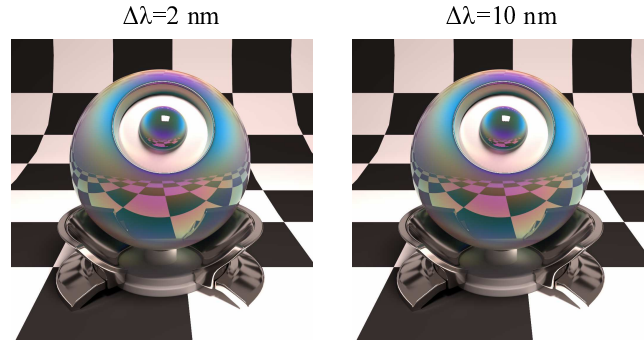
Supplementary Figure 17: Rendered images for the spherical probe computed at two different spectral resolutions. The disordered metasurface is a monolayer of silver particles of radius $r = 90$ nm on a SiO_2/Si substrate with $h = 400$ nm with a surface coverage $f = 0.1$ and a correlation degree $p = 0.5$. The two rendered images for a 2 nm resolution (left) and a 10 nm resolution (right) are indistinguishable by eye. This justifies the 10 nm resolution used for the numerical computations in this work.


$\Delta\theta$=0.5°, $\Delta\varphi$=1° $\Delta\theta$=1°, $\Delta\varphi$=1° $\Delta\theta$=1°, $\Delta\varphi$=2°
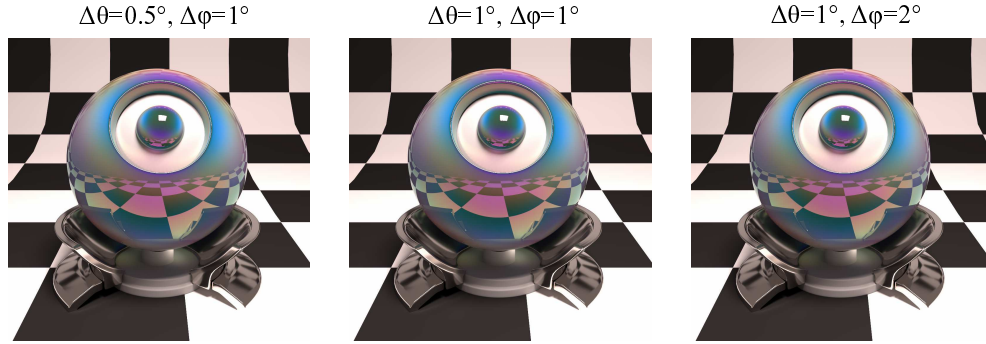
Supplementary Figure 18: Rendered images for the spherical probe computed at three different angular resolutions. We hardly notice any difference by eye when the original angular resolution (0.5° and 1° for the zenith and azimuth angles, left image) is degraded (middle and right images). This fully justifies the angular resolution used for the numerical computations in this work.

SUPPLEMENTARY NOTE 5. QUANTITATIVE BRDF MEASUREMENTS ON DISORDERED METASURFACES

In addition to the appearance acquisition of the two centimetre-scale metasurfaces (Fig. 5 of the main text), we perform quantitative BRDF measurements of the two samples. The BRDFs are recorded with a home-made spectrogoniometre setup calibrated with a Lambertian diffusor using a supercontinuum laser as a source. Supplementary Figure 19 shows normalized measurements performed as a function of the wavelength λ and the detection zenith angle θ. The samples are illuminated with an angle of incidence $\theta_i = 30°$. To avoid blocking the incident light for a large set of angles, the measurements are performed 20° above the plane of incidence. Note that the black stripe at $\theta \approx 20°$ comes from the detector support blocking the incident laser.

As expected, the spectra reveal the presence of Mie resonances that produce the diffuse colours observed in Fig. 5 of the main text. The spectral shift between the weakly and strongly correlated media, which induces a variation of the diffuse colour between the two samples, is due to the ageing of the negative resist, which has been used for the fabrication of the two samples, over an interval of two months. More importantly, for the weakly correlated metasurface ($p = 0.1$), the reflection peak extends over the complete set of detection angles with a small redshift as θ decreases, whereas for the strongly correlated metasurface ($p = 0.5$), nearly all the reflected intensity in the detection plane is collected in backreflection around angles centered on $\theta \approx 50°$, in full consistency with the appearance acquisitions reported in Fig. 5 and with the numerical predictions of Supplementary Fig. 11.
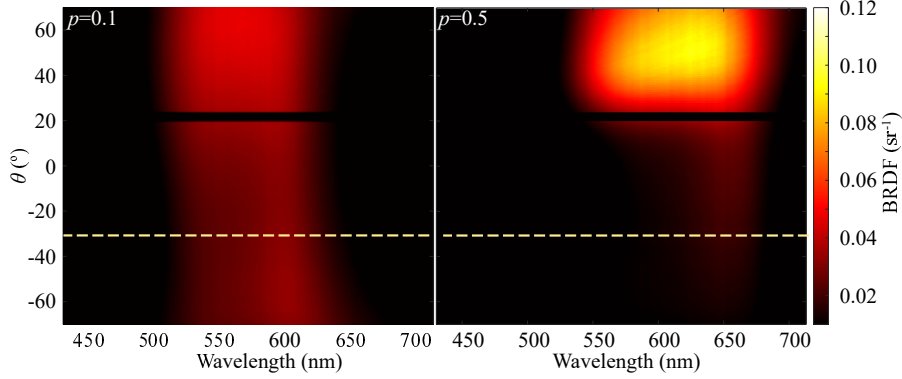
Supplementary Figure 19: Quantitative BRDF measurement on disordered metasurfaces with varying structural correlations. The BRDF spectra are measured 20° above the plane of incidence for light incident at $\theta_i = 30°$. Short-range structural correlations lead to a suppression of the diffuse intensity near the specular direction $\theta \approx -30°$ (yellow dashed line) and an increase in backscattering around $\theta = 50°$.

SUPPLEMENTARY REFERENCES

[S1] L. Tsang and J. A. Kong, *Scattering of electromagnetic waves: advanced topics*, (John Wiley & Sons, 2004).

[S2] M. I. Mishchenko, L. D. Travis, and A. A. Lacis, *Multiple scattering of light by particles: radiative transfer and coherent backscattering* (Cambridge University Press, 2006).

[S3] C. F. Bohren and D. R. Huffman, *Absorption and scattering of light by small particles* (John Wiley & Sons, 2008).

[S4] M. I. Mishchenko, L. D. Travis, and D. W. Mackowski, J. Quant. Spectrosc. Radiat. Transf. **55**, 535 (1996).

[S5] C.-T. Tai, *Dyadic Green functions in electromagnetic theory* (Institute of Electrical & Electronics Engineers (IEEE), 1994).

[S6] A. García-Valenzuela, E. Gutiérrez-Reyes, and R. G. Barrera, J. Opt. Soc. Am. A **29**, 1161 (2012).

[S7] N. A. Loiko, A. A. Miskevich, and V. A. Loiko, J. Opt. Soc. Am. A **35**, 108 (2018).

[S8] K. Sasihithlu, N. Dahan, J.-P. Hugonin, and J.-J. Greffet, J. Quant. Spectrosc. Radiat. Transf. **171**, 4 (2016).

[S9] J. Yang, J.-P. Hugonin, and P. Lalanne, ACS Photon. **3**, 395 (2016).

[S10] S. Torquato and H. Haslach Jr, Appl. Mech. Rev. **55**, B62 (2002).

[S11] M. Baus and J.-L. Colot, Phys. Rev. A **36**, 3912 (1987).

[S12] M. Pharr, W. Jakob, and G. Humphreys, *Physically based rendering: From theory to implementation* (Morgan Kaufmann, 2016).

[S13] M. Bertrand, A. Devilez, J.-P. Hugonin, P. Lalanne, and K. Vynck, J. Opt. Soc. Am. A **37**, 70 (2020).

[S14] A. Jouanin, J. P. Hugonin, and P. Lalanne, Adv. Funct. Mater. **26**, 6215 (2016).

[S15] W. Mokrzycki and M. Tatol, Mach. Graph. Vis **20**, 383 (2011).